Journal of Materials Chemistry B

ROYAL SOCIETY OF CHEMISTRY

PAPER

View Article Online
View Journal | View Issue

Cite this: J. Mater. Chem. B, 2021, 9, 6076

Multiscale pore contained carbon nanofiber-based field-effect transistor biosensors for nesfatin-1 detection†

Sung Gun Kim[a] and Jun Seop Lee *[b]

Received 18th March 2021,
Accepted 30th June 2021

DOI: 10.1039/d1tb00582k

rsc.li/materials-b

Nesfatin-1 (NES1) is a potential biomarker found in serum and saliva that indicates hyperpolarization and depolarization in the hypothalamic ventricle nucleus as well as an increase in epileptic conditions. However, real-time investigations have not been carried out to detect changes in the concentration of NES1. In this study, we develop a multiscale pore contained carbon nanofiber-based field-effect transistor (FET) biosensor to detect NES1. The activated multiscale pore contained carbon nanofiber (a-MPCNF) is generated using a single-nozzle co-electrospinning method and a subsequent steam-activation process to obtain a signal transducer and template for immobilization of bioreceptors. The prepared biosensor exhibits a high sensitivity to NES1. It can detect levels as low as 0.1 fM of NES1, even in the presence of other interfering biomolecules. Furthermore, the a-MPCNF-based FET sensor has significant potential for practical applications in non-invasive real-time diagnosis, as indicated by its sensing performance in artificial saliva.

1. Introduction

Epilepsy is a global health concern and one of the most difficult conditions to diagnose. For the diagnosis of epilepsy, electroencephalogram (EEG) measurements are beneficial in addition to investigating the clinical history of the symptoms of seizures. However, practical diagnosis is still a difficult task as EEG with sophisticated instruments is expensive for patients and sometimes cannot even provide a definitive diagnosis, which leads to nonpathological consequences.[1–4] Recently, it has been reported that a relationship exists between animal and human hormones and seizures; changes in serum hormone levels have been associated with temporary deformation during seizures, affecting brain function, metabolism, and temporal epilepsy secretion.[5–8] Although diagnostic methods for epilepsy have been reported in several studies, including the diagnostic potential of serum prolactin levels, its sensitivity and specificity for the diagnosis of epileptic seizures remain controversial.[9–11]

Nesfatin-1 (NES1) is involved in various physiological functions, including food intake, stimulation of appetite, and energy homeostasis, with a decreased expression in the hypothalamic ventricle nucleus (PVN) during starvation.[12–14] In addition, electrophysiological studies have shown that NES1 stimulates hyperpolarization and depolarization in PVN neurons and in the arcuate nucleus (ARC) and that NES1, found in serum and saliva, is a potential biomarker of increased epilepsy.[15–18] Currently, in addition to EEG, increased prolactin levels are used to distinguish epileptic seizures from nonepileptic events.[19,20] However, in this regard, the use of prolactin has several limitations, such as the fact that it should be measured 10–20 min after the event and that it is not suitable for use in conditions such as status epilepsy, repetitive seizures, and neonatal seizures.[21–23] The levels of NES1 have been reported to increase in real-time in patients with epilepsy and thus may be useful in identifying individuals suffering from epileptic seizures.[24]

Precise sensing platforms for the detection of appropriate biomarkers have become increasingly important for monitoring human diseases, food safety, and hazardous elements.[25–28] Among them, a field-effect transistor (FET)-based sensor using a bioreceptor (such as an aptamer or antibody) is most commonly used since it can be employed to acquire a change in signal in real-time with high sensitivity.[29–31] Carbon nanomaterials are often used for the charge-transfer channel in FET biosensors since they can be easily modified using a variety of covalent or π-stacking methods to immobilize the bioreceptors.[32–35]

[a] Samsung Electronics, San #16 Banwol-Dong, Hwasung, Gyeonggi-Do18448, South Korea
[b] Department of Materials Science and Engineering, Gachon University, 1342 Seongnam-Daero, Sujeong-Gu, Seongnam-Si, Gyeonggi-Do 13120, Republic of Korea. E-mail: junseop@gachon.ac.kr; Fax: +82-31-750-5389; Tel: +82-31-750-5814

† Electronic supplementary information (ESI) available: Electrospinning mechanism of the polymer solution; BET surface area and BJH pore distribution of CNFs; comparison XPS C 1s spectra of a-MPCNFs; morphology of Ab-a-CNF; C 1s XPS of Ab-a-MPCNF-10; IV curve of a-CNF-10 based electrode; real-time signal change in the NES1 response; sensing performance of carbon-based nanomaterials; selectivity test of the electrode among peptide hormones; sensing performance of Ab-a-CNF in artificial saliva. See DOI: 10.1039/d1tb00582k

In particular, 1D carbon nanostructures have been shown to be particularly effective due to their increased charge-transfer properties and large surface-to-volume ratio, which are critical factors for increasing the sensitivity of the sensing electrode.[36,37] As 1D carbon structures, carbon nanofibers (CNFs), generated from electrospinning, are promising for sensing applications since their electrochemical properties and structures can be easily controlled by varying the processing conditions and precursor composition.[38–40] However, research on how the functional group can be introduced while changing the carbon microstructure, without the loss of electrochemical and structural benefits, is still limited.

Here, we report the fabrication of a FET-based biosensor for NES1, with nesfatin-1 antibody (anti-NES1) immobilized activated multiscale pore contained carbon nanofibers (Ab-a-MPCNFs) using single-nozzle co-electrospinning and a steam-activation process. First, multicore polymer nanofibers consisting of poly(methyl methacrylate) (PMMA) (for the core) and poly(acrylonitrile) (PAN) (for the shell) were generated through electrospinning of the mixed polymer solution. The activated multiscale pore contained carbon nanofibers (a-MPCNFs) were then formed after the heat treatment step, in combination with carbonization and steam activation. In particular, the amount of functional groups and micropores in the carbon structure was controlled by changing the time of exposure to H_2O vapor. Finally, anti-NES1 was immobilized onto the a-MPCNF surface, and a FET-type sensing electrode was assembled with a liquid-ion gate configuration. The electrode of the biosensor exhibits a high sensitivity to NES1, exhibiting a low limit of detection (LOD) of 0.1 fM and a fast detection time (<1 s) owing to the multiscale porous structure. Moreover, this biosensor can distinguish NES1 from artificial saliva, thus illustrating its potential in non-invasive diagnosis of epileptic seizures.

2. Experimental section

2.1 Materials

All chemicals were used as received without any further purification. Poly(acrylonitrile) (PAN, Mw 150 000), poly(methyl methacrylate) (PMMA, Mw 350 000), 4-(4,6-dimethoxy-1,3,5-triazin-2-yl)-4-methylmorpholinium chloride (DMT-MM), and 3-aminopropyltrimethoxysilane (APS) were purchased from Sigma-Aldrich. *N*,*N*-Dimethylformamide (DMF) (Sigma-Aldrich) was used as the solvent for both the PAN and PMMA solutions. NES1 and anti-NES1 were purchased from LSBio. The anti-NES1 stock solution was diluted with a PBS buffer solution (pH 7.4) and was stored at −20 °C until use. Recombinant hepatitis B virus surface antigen protein was purchased from Abcam. The commercial artificial saliva for xerostomia was used as the saliva solution sample.

2.2 Fabrication of the a-MPCNF-based biosensor

As a signal transducer, a-MPCNFs were fabricated *via* electrospinning, carbonization, and subsequent steam activation. In detail, 10 wt% PAN solution was prepared in a DMF solvent at 60 °C followed by vigorous stirring for 2 h. PMMA solution was also prepared in the same manner as the PAN solution. The mixed polymer solution (1 : 1 mass ratio of PAN:PMMA) was electrospun using a single syringe nozzle with an applied voltage of 18 kV to generate multicore nanofibers. Then, the electrospun nanofibers were stabilized at 270 °C for 1 h in air, carbonized under an argon (Ar) flow at 700 °C for 1 h and then activated for different durations with exposure to H_2O under an Ar flow at 800 °C.

To develop the bioreceptor-modified a-MPCNF FET-based biosensor, the amino silane (APS) coated electrode was fabricated as the first step. In detail, an interdigitated array (IDA) electrode was treated with aqueous APS (5 wt%) for 6 h to introduce amino groups to the electrode surface. The treated electrode was then exposed to a mixture of a-MPCNFs solution (40 μL, 0.1 wt%) and DMT-MM aqueous solution (40 μL, 1 wt%) at 25 °C for 12 h. Subsequently, the coupling reaction to attach the anti-NES1 to the a-MPCNF surface was carried out using a mixture of the antibody (0.1 mM) solution and DMT-MM aqueous solution (40 μL, 1 wt%) for 12 h. The electrode was then repeatedly rinsed with distilled water and dried at 25 °C for 12 h.

2.3 Characterization

Field-emission scanning electron microscopy (FE-SEM) images were obtained using a JEOL-6700 (JEOL) (JEOL Ltd, Tokyo, Japan) installed at the Chemical and Biological Engineering Research Facilities at Seoul National University. Transmission electron microscopy (TEM) images were obtained using a JEM-2100 installed at the National Center for Inter-University Research Facilities at Seoul National University. Nitrogen adsorption–desorption isotherms were analyzed using an ASAP 2010 (Micrometrics) equipment. The pore size distribution and surface area were measured *via* the Brunauer–Emmett–Teller (BET) and Barrett–Joyner–Halenda (BJH) methods. FT-IR spectra were collected with a Spotlight 200i Frontier (PerkinElmer) spectrophotometer in attenuated total reflection mode. XPS spectra were recorded using an Axis-His system (KRATOS).

2.4 Investigation of the sensing performance

All electrical measurements were carried out using a Keithley 2612A source meter and a probe station (MS TECH, model 4000). A 300 μL chamber was used for the solution-based measurements. The change in the current was normalized as follows:

$$[\Delta I/I_0]_{SD}(\%) = \frac{I - I_0}{I_0} \times 100$$

The artificial saliva was produced according to the published recipe as follows: 25 mM K_2HPO_4 (0.1 L), 24 mM Na_2HPO_4 (0.1 L), 150 mM $KHCO_3$ (1 L), 1.5 mM $MgCl_2$ (0.1 L), 100 mM NaCl (0.1 L), 25 mM citric acid (0.006 L), and 5 mM $CaCl_2$ (0.1 L).[22] Furthermore, the commercially available oral rinse (Biotene, GSK, USA) was added to give a viscosity similar to actual saliva.

3. Results and discussion

3.1 Fabrication of a-MPCNFs

For the conductive channel of the sensing electrode, a-MPCNFs were generated *via* the single-nozzle co-electrospinning method

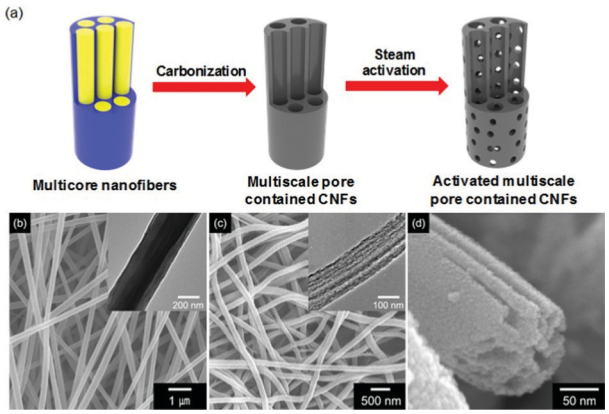

Fig. 1 (a) Illustration of the sequential fabrication steps for the activated multiscale pore contained carbon nanofibers (a-MPCNFs). Field-emission scanning electron microscopy (FE-SEM) and transmission electron microscopy (TEM) (inset) images of (b) electrospun multicore nanofibers and (c) a-MPCNFs. (d) A cross-sectional FE-SEM image of a-MPCNFs.

followed by a steam-activation process (Fig. 1a). First, a polymer solution composed of PAN and PMMA was electrospun through a single nozzle. During electrospinning of this mixed solution, discrete droplets of PMMA elongate along the inside of the PAN shell due to the stretching force of the applied voltage, leading to the formation of multicore nanofibers with a diameter of ~300 nm (Fig. S1, ESI† and Fig. 1b). The phase-separated polymer nanofibers were then stabilized at 270 °C for 1 h in air and carbonized at 700 °C for 1 h under an argon (Ar) atmosphere. During these two steps, the continuous PAN phase was transformed into carbon while the inner elongated PMMA phase decomposed, resulting in the formation of an internal multichannel.[41] Owing to the elimination of PMMA from within the fibers, the multicore nanofibers are constricted during the heating process. Moreover, exposure to H_2O under an Ar flow was carried out to functionalize the surface of carbon. Eventually, the a-MPCNFs were found to be well fabricated, exhibiting well-defined structures without any collapse of the channels, as shown in Fig. 1c and d. In addition, the structure and quantity of the carboxyl functional groups were optimized by controlling the activation time. In particular, the thickness of the carbon structures was decreased by limiting the activation time up to 10 min, whereas a longer activation time resulted in the collapse of the outer carbon structure (Fig. 2).

To investigate the microstructure of carbon nanostructures, Brunauer–Emmett–Teller (BET) and Barrett–Joyner–Halenda (BJH) analyses were conducted. Fig. 3a illustrates the adsorption/desorption isotherms of nitrogen (N_2) for the MPCNFs with different activation times. The isotherms of a-MPCNFs display a type IV hysteresis that consists of micropores at low relative pressures (0–0.2 P/P_0), originating from the steam activation, and mesopores at high relative pressures (>0.8 P/P_0), originating from the multichannel structure. The surface area increases as the steam-activation time increases by up to 10 min (798.3 $m^2\ g^{-1}$ for 0 min (MPCNF); 1101.4 $m^2\ g^{-1}$ for 5 min (a-MPCNF-5); and 1350.7 $m^2\ g^{-1}$ for 10 min (a-MPCNF-10)).

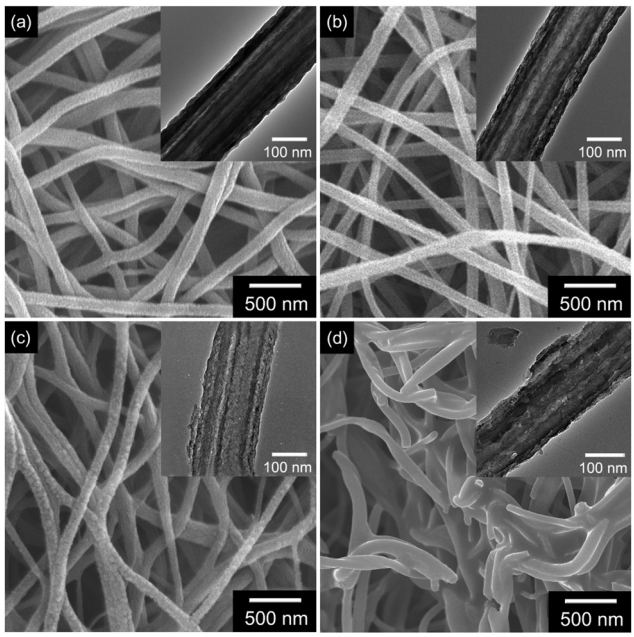

Fig. 2 FE-SEM and TEM (inset) images of a-MPCNFs with different activation times: (a) 0 min, (b) 5 min, (c) 10 min, and (d) 15 min.

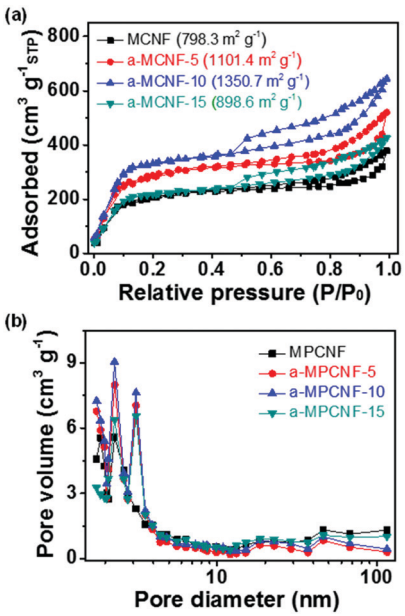

Fig. 3 (a) Nitrogen adsorption–desorption and (b) pore size distribution curves of the a-MPCNFs with different activation times: 0 min (black), 5 min (red), 10 min (blue), and 15 min (green).

However, more than a 10 min activation time decreases the surface area (898.6 $m^2\ g^{-1}$ for 15 min (a-MPCNF-15)) due to the collapse of the structure. Moreover, the pore distribution was measured *via* the BJH method, as shown in Fig. 3b. Regarding the pore distribution of carbon, the peak at *ca.* 20 nm illustrates the presence of an inner hollow multichannel in the structure, whereas the peaks at 1.8 and 2.3 nm indicate the existence of small pores originating from the thermal decomposition of the

PMMA phase. As the steam-activation time reaches 10 min, the pore distribution peaks at 1.8 and 2.3 nm increase, and a peak at 3.1 nm is observed because of the etching of carbon, as a result of the activation. Thus, the multichannel and small pores in the carbon structure can lead to an increase in the amount of immobilized receptors without aggregation. On the other hand, a 15 min activation time decreases the volume of micropores due to the collapse of the structure. In the case of CNF, the longer activation process time increases the surface area and the volume of the micropores (Fig. S2, ESI†). However, the CNF not only has a smaller surface area than MPCNF, but it is also limited to types of micropores around 2 nm.

Fourier-transform infrared (FT-IR) spectra for a-MPCNFs are presented in Fig. 4. Functionalization of MPCNFs is confirmed by the presence of peaks associated with oxygen, including the C═O stretching peak at 1720 cm^{-1}, the stretching vibration and deformation peaks of –OH groups at 3430 and 1400 cm^{-1}, respectively, and the stretching vibration peaks of C–O bonds (including those in phenol groups) at 1080 and 1230 cm^{-1}. The peak at 1590 cm^{-1} corresponds to the structural lattice vibrations of the carbon nanofibers and indicates that the structure of the a-MPCNFs remains intact after activation treatment. The increase in the intensity of the characteristic peaks at 1230, 1720, and 3430 cm^{-1} suggests that the carboxyl groups are properly formed on the surface of the MPCNFs as the activation time increases.

The chemical composition of a-MPCNFs was also investigated *via* X-ray photoelectron spectroscopy (XPS). Fig. 5 displays high-resolution XPS spectra for the C (1s) region around 284.5 eV; these peaks were deconvoluted into the following component peaks: C═C and C–C (284.3 eV) in the aromatic rings, C–O (286.5 eV) in the epoxy and hydroxyl groups, and C═O (288.0 eV) derived from the carbonyl and carboxyl groups. An increase in the intensity of the peak associated with the carboxyl groups was observed by comparing the intensity of the peaks corresponding to the oxygen-related functional groups. This demonstrates that the intensity ratios, I_{C-O} and $I_{C=O}$, gradually increase as the activation time increases owing to an increase in the quantity of oxygen in the a-MPCNFs (Table S1, ESI†). These spectral investigations indicate that the carboxyl groups were well functionalized on the MPCNFs after the steam-activation process.

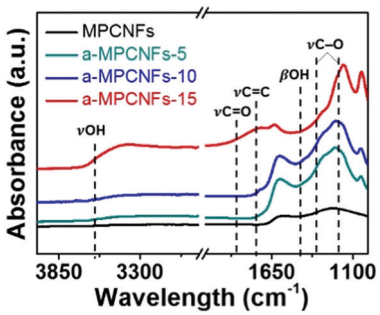

Fig. 4 Fourier-transform infrared spectra of the a-MPCNFs with different activation times (black: 0 min, green: 5 min, blue: 10 min, and red: 15 min).

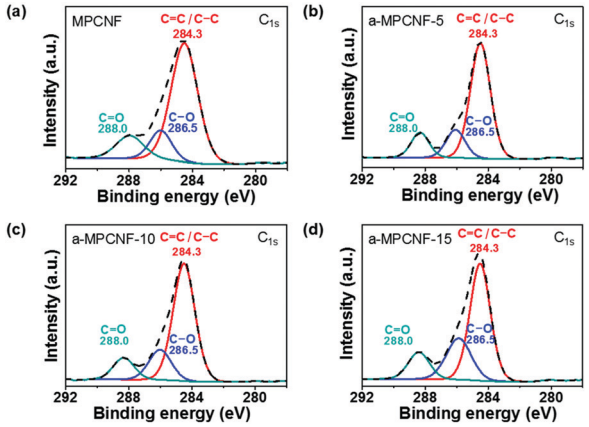

Fig. 5 X-ray photoelectron spectra of C 1s of the a-MPCNFs with different activation times: (a) 0 min, (b) 5 min, (c) 10 min, and (d) 15 min.

3.2 Fabrication of the Ab-a-MPCNF-based biosensor

Due to the large surface area and the presence of the carboxyl functional group on the surface, a-MPCNF-10 was used as the conductive channel of the sensing electrode. First, a-MPCNF-10 was located between anti-NES1 and the electrode as a sensing transducer *via* covalent bonding of the functional groups. Fig. 6 depicts a schematic illustrating the formation of the receptor-modified a-MPCNF-10 on the electrode substrate. The amine-functionalized electrode and carboxyl-functionalized a-MPCNF form an amide bond through an organic catalysis reaction.[42] In addition, the anti-NES1 is immobilized onto the a-MPCNF-10 surface *via* the same reaction. Fig. 7a illustrates the anti-NES1 immobilized onto a-MPCNF-10 (Ab-a-MPCNF-10) on the sensing electrode. The morphology of Ab-a-MPCNF-10 is confirmed through the decoration of anti-NES1 in the carbon structure without aggregation, owing to micro-/mesopores in the carbon (Fig. 7b). Anti-NES1 is also uniformly distributed on the carbon surface based on the amide bond after the activation process (Fig. S3, ESI†). However, there is little distribution of

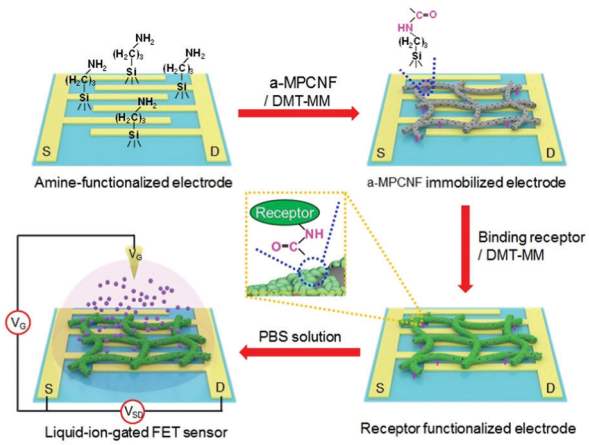

Fig. 6 Schematic illustration of the fabrication steps for the activated multiscale pore contained carbon nanofiber (a-MPCNF)-based liquid-ion gated FET-type biosensor.

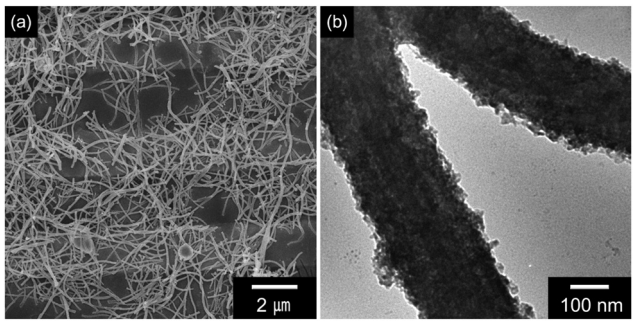

Fig. 7 (a) FE-SEM image of the binding receptor functionalized a-MPCNF (Ab-a-MPCNF)-based sensor electrode. (b) TEM image of the Ab-a-MPCNF.

micropores, which results in less uniformity than MPCNF. In addition, the C 1s XPS spectra of Ab-a-MPCNF-10 suggest a new peak at 286 eV (C–N) that indicates the formation of an amide bond after anti-NES1 immobilization (Fig. S4, ESI†). Finally, phosphate buffer solution (PBS) was added *via* a small chamber to prepare the liquid-ion gate sensing system.

3.3 Characterization of the biosensor electrode

Fig. 8 indicates the current–voltage (*I–V*) characteristics of anti-NES1 immobilized carbon nanofiber-based electrodes that employ the activated carbon nanofiber from only PAN (a-CNF-10) and a-MPCNF-10. Both before and after being modified with the antibody, these *I–V* characteristics exhibit a linear trend in the voltage range from −0.1 to 0.1 V. This indicates that the conductive transducer materials form Ohmic contacts with the electrodes. As the anti-NES1 provides resistance, the value of d*V*/d*I* increases in proportion to the concentration of the modifying antibody. However, the order of d*V*/d*I* does not change, and the linear Ohmic properties are maintained after immobilization of the antibody. These results suggest that the covalent immobilization of the antibody is successful and that the electrical contacts are reproducible. In addition, the slope of a-MPCNF-10-based electrodes is slightly lower than that of a-CNF-10. This is due to the destroyed sp^2 carbon structure caused by the decomposition of PMMA, which contributes to electrical conductivity. In addition, Fig. 8b and Fig. S5 (ESI†) indicate the source–drain current (I_{SD}) as a function of the source–drain bias (V_{SD}) under various gate biases (V_G) for the liquid-ion-gated FET devices, formed using Ab-a-MPCNF-10 and the antibody modified a-CNF-10 (Ab-a-CNF-10). The *I–V* measurements indicate that I_{SD} increases (*i.e.*, becomes more negative) as V_G is decreased from +0.8 to −0.8 V, indicating p-type behaviour (*i.e.*, hole transport). Varying V_G alters the oxidation state of the sp^2 carbon and the charge carrier distribution.

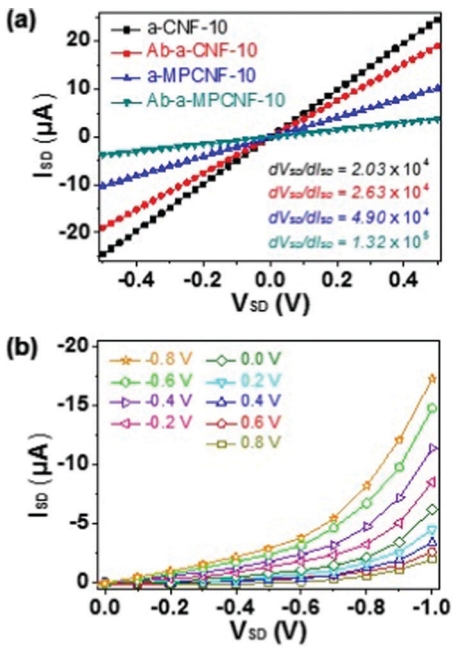

Fig. 8 (a) Source–drain current–voltage (I_{SD}–V_{SD}) curves of carbon nanofiber-based FET sensor electrodes: a-CNF (black), Ab-a-CNF (red), a-MPCNF (blue), and Ab-a-MPCNF (green). (b) I_{SD}–V_{SD} characteristics of Ab-a-MPCNF-10-based FET sensor electrodes ($-0.8\ V \le V_G \le +0.8\ V$ in steps of 0.2 V with a V_{SD} scan rate of 10 mV s^{-1}).

3.4 Real-time response of the biosensor

To evaluate the sensing characteristics of the electrodes, changes in I_{SD} were monitored in real-time, with V_G = 50 mV and V_{SD} = 50 mV, while introducing solutions containing various concentrations of NES1 in PBS. Fig. 9a shows the real-time response of Ab-a-CNF-10 and Ab-a-MPCNF-10 biosensors. Following the injection of NES1, I_{SD} decreases rapidly within *ca.* 1 s and saturates thereafter (Fig. S6, ESI†). The decrease in I_{SD} is caused by the interaction between NES1 and the antibody during the formation of the antibody–NES1 complex. NES1 specifically binds to Ab-a-MPCNF-10 due to the intermolecular interaction with the target compounds. The formation of the antibody–target complex influences the negative charge density at the surface of the carbon structure. This changes the charge-transport properties of the carbon-based conductive channels that may decrease the hopping rate of charge carriers, resulting in a decrease in I_{SD}. The sensing capacity of Ab-a-MPCNF-10 is higher than that of Ab-a-CNF-10 because the micro-/meso-porous structure of carbon increases the amount of antibody covered in carbon. This result indicates that the change in the surface charge density affects Ab-a-MPCNF-10 to a greater extent than Ab-a-CNF-10. For this reason, the Ab-a-MPCNF-10 electrode was able to detect NES1 more rapidly with a remarkably low LOD of 0.1 fM (a signal-to-noise ratio of $\geq$3.0) which is much higher ($\sim 10^5$ fold) than that of conventional carbon nanomaterial-based biosensors (Table S2, ESI†).

Fig. 9b illustrates the sensitivity (S) of the electrodes as a function of the concentration of NES1. The sensitivity was determined from the normalized change in the current (*i.e.*, the saturation level of $[\Delta I/I_0]_{SD} \times 100$ measured after exposure to the analyte for 10 s). Salivary NES1 is normally secreted at levels ranging from 2 pM ± 300 fM; however, it remarkably increases to 340 pM ± 29 pM in the saliva of epileptic patients.[23] Therefore, a biosensor for salivary NES1 should cover the range from 1 to 1000 pM. The sensitivity of the Ab-a-MPCNF-10 sensor to NES1 in PBS linearly increases with the concentration, over a

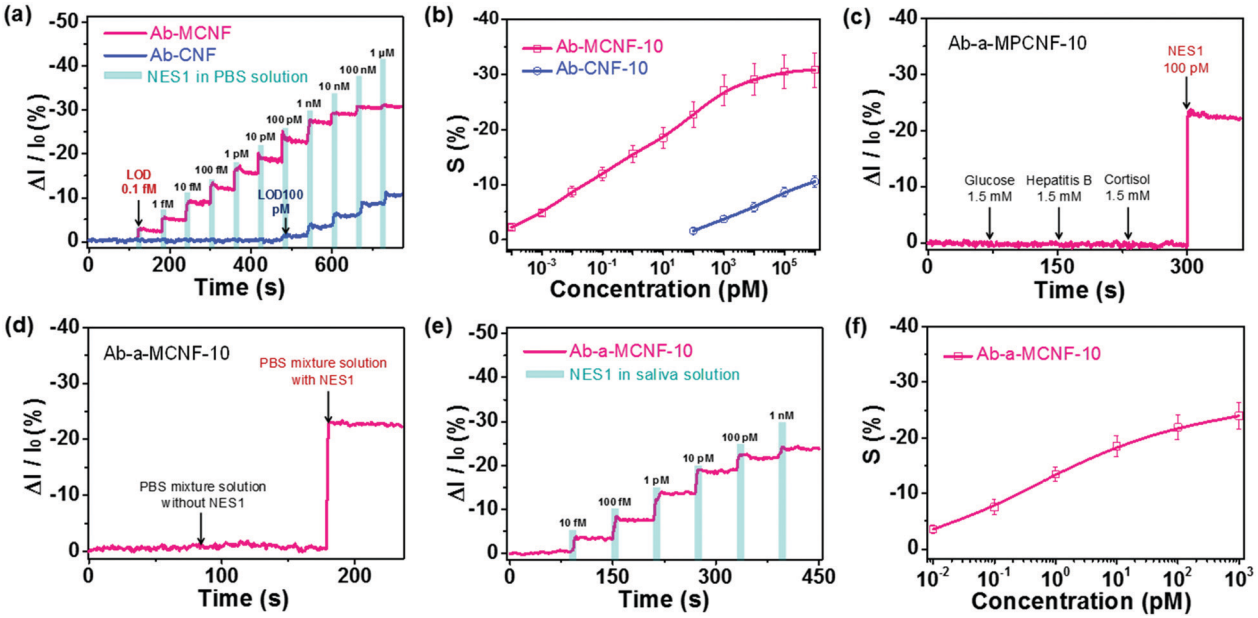

Fig. 9 (a) Real-time responses of the normalized current of Ab-a-CNFs and Ab-a-MPCNF-based FET sensors (gate bias: V_G = 50 mV and source–drain bias: V_{SD} = 50 mV). (b) Calibration curves of FET sensors formed as a function of NES1 concentration (detection of NES1 was conducted 5 times for every concentration. Error bars originated from the standard deviation method.). A real-time response of the Ab-a-MPCNF FET sensor (c) to non-target (glucose, hepatitis B, and cortisol) and target (NES1) and (d) to various analytes before and after being mixed with NES1. (e) A real-time response of the normalized current and (f) the calibration curve of the Ab-a-MPCNF FET sensor at various concentrations of NES1 in the artificial saliva solution (detection of NES1 was conducted 5 times for every concentration. Error bars originated from the standard deviation method.).

wide concentration range of 10^{-5}–10^{7} pM, which covers the physiological range of the NES1 concentration (up to pM) in real saliva.

The specificity of the Ab-a-MPCNF-10 sensor was examined using nontarget samples (glucose, hepatitis B, and cortisol), which can be found in real saliva. The Ab-a-MPCNF-10 sensor exhibits negligible changes in I_{SD} following exposure to a 1.5 mM solution containing the nontarget molecules. However, a much larger change in the signal occurs immediately after exposure to a 100-pM solution of NES1, as shown in Fig. 9c. In addition, 1.5 mM solutions of mixed nontarget molecules were prepared with and without 100 pM of BPA and were added consecutively and individually to further investigate the specificity. As presented in Fig. 9d, a significant change in I_{SD} can be observed only upon introducing the mixtures containing NES1, thereby demonstrating the high specificity of this sensor to NES1. The Ab-a-MPCNF-10 sensor also displays excellent sensitivity to NES1 even in the presence of other peptide hormones (insulin, glucagon, oxytocin, corticotropin, and thyrotropin) (Fig. S7, ESI†).

Additionally, to confirm the feasibility of the diagnosis of epilepsy, the detection of NES1 was conducted in artificial saliva as the electrolyte. As shown in Fig. 9e and f, the Ab-a-MPCNF-10 sensor exhibits a detection limit of 10 fM with a wide dynamic sensing range (10 fM–1 nM), including that for normal and epileptic patients (2 pM–340 pM).[23] NES1 was also measured in an artificial saliva solution using Ab-a-CNF and detected concentrations ranging from 500 pm to 500 nM (Fig. S8, ESI†). This concentration range, unlike in the case of

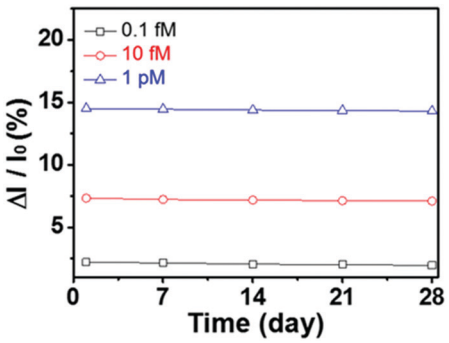

Fig. 10 Sensing performance comparison of the Ab-a-MPCNF sensor to NES1 over 4 weeks of storage. Measurements were obtained at 1 week intervals.

Ab-a-MPCNF, cannot detect changes in patients with epilepsy due to seizures.

Fig. 10 suggests an estimation of the stability of the Ab-a-MPCNF electrode over several weeks. To confirm stability, the Ab-a-MPCNF electrode was stored in a sealed vessel at 25 °C for 4 weeks under air-dried conditions. The response of the electrode is displayed with 0.1 fM, 10 fM, and 1 pM of NES1. Under these conditions, the response current decreases less than 5% after 4 weeks, which originates from the deactivation of anti-NES1.[43]

4. Conclusions

In summary, an anti-NES1-modified a-MPCNF-based biosensor was developed *via* a co-electrospinning method and subsequent

steam-activation process. The highly porous carbon structure enhances the amount of the bioreceptor covered on the sensor electrode and increases its affinity to the target analyte (NES1 molecule). As a result, the Ab-a-MPCNF sensor electrode exhibits a high sensitivity (down to 0.1 fM) to NES1, which is much higher ($\sim 10^5$ fold) than that of conventional carbon nanomaterial-based sensors. Moreover, the Ab-a-MPCNF FET sensor displays a high selectivity to NES1 in mixtures with interfering molecules and artificial saliva. Thus, the results of the present work indicate an effective method for the fabrication of FET-based biosensors with high sensitivity using porous carbon nanostructures.

Author contributions

S. G. Kim contributed to the conceptualization, methodology, validation, formal analysis, and writing – original draft and J. S. Lee contributed to the supervision, writing – original draft, and writing – review and editing.

Conflicts of interest

There are no conflicts to declare.

Acknowledgements

This work was supported by the National Research Foundation of Korea (NRF) grant funded by the Korea government (MSIT) (No. 2020R1A4A407983711).

Notes and references

1 S. Ramgopal, S. Thome-Souza, M. Jackson, N. E. Kadish, I. S. Fernández, J. Klehm, W. Bosl, C. Reinsberger, S. Schachter and T. Loddenkemper, Seizure detection, seizure prediction, and closed-loop warning systems in epilepsy, *Epilepsy Behav.*, 2014, **37**, 291–307.

2 Q. Zhang, J. Ding, W. Kong, Y. Liu, Q. Wang and T. Jiang, Epilepsy prediction through optimized multidimensional sample entropy and Bi-LSTM, *Biomed. Signal Process. Control*, 2021, **64**, 102293.

3 M. El-Hallal, Y. Shah, M. Nath, P. Eksambe, L. Theroux, M. Amlicke, F. Steele, W. Krief and S. Kothare, Length of stay linked to neurodiagnostic workup for seizures presenting to the pediatric emergency department, *Epilepsy Behav.*, 2021, **115**, 107639.

4 K. H. Ha, A. C. Schomer, J. Leonardo and M. Quigg, Time of day is an inaccurate surrogate marker for sleep-wake state in an epilepsy monitoring unit, *Epilepsy Res.*, 2021, **169**, 106524.

5 W. Loscher, Animal models of intractable epilepsy, *Prog. Neurobiol.*, 1997, **53**, 239–258.

6 M. Fu, J. Tao, D. Wang, Z. Zhang, X. Wang, Y. Ji and Z. Li, Downregulation of microRNA-34c-5p facilitated neuroinflammation in drug-resistant epilepsy, *Brain Res.*, 2020, **1749**, 147130.

7 S. Bröer, Not part of the temporal lobe, but still of importance? Substantia nigra and subthalamic nucleus in epilepsy, *Front. Syst. Neurosci.*, 2020, **14**, 581826.

8 Y. Li, S. Chen, J. Qin, Y. She, Y. Chen, X. Liu, H. Yu and L. Zhou, Risk of seizure recurrence from antiepileptic drug withdrawal among seizure-free patients for more than two years, *Epilepsy Behav.*, 2020, **113**, 107485.

9 R. D. Nass, R. Sassen, C. E. Elger and R. Surges, The role of postictal laboratory blood analyses in the diagnosis and prognosis of seizures, *Seizure*, 2017, **47**, 51–65.

10 E. Clynen, A. Swijsen, M. Raijmakers, G. Hoogland and J.-M. Rigo, Neuropeptides as targets for the development of anticonvulsant drugs, *Mol. Neurobiol.*, 2014, **50**, 626–646.

11 E. Oribe, R. Amini, E. Nissenbaum and B. Boal, Serum prolactin concentrations are elevated after syncope, *Neurology*, 1996, **47**, 60–62.

12 H. Shimizu, S. Oh-I, S. Okada and M. Mori, Nesfatin-1: an overview and future clinical application, *Endocr. J.*, 2009, **56**, 537–543.

13 C. D. Fjell, J. A. Hiss, R. E. W. Hancock and G. Schneider, Designing antimicrobial peptides: form follows function, *Nat. Rev. Drug Discovery*, 2012, **11**, 37–51.

14 A. M. Blanco, J. I. Bertucci and S. Unniappan, FGF21 mimics a fasting-induced metabolic state and increases appetite in zebrafish, *Sci. Rep.*, 2020, **10**, 6993.

15 S. Aydina, E. Dag, Y. Ozkan, O. Arslan, G. Koc, S. Bek, S. Kirbas, T. Kasikci, D. Abasli, Z. Gokcil, Z. Odabasi and Z. Catak, Time-dependent changes in the serum levels of prolactin, nesfatin-1 and ghrelin as a marker of epileptic attacks young male patients, *Peptides*, 2011, **32**, 1276–1280.

16 R. Dore, L. Levata, H. Lehnert and C. Schulz, Nesfatin-1: functions and physiology of a novel regulatory peptide, *J. Endocrinol.*, 2017, **232**, R45–R65.

17 K. Fang, H.-R. Li, X.-X. Chen, X.-R. Gao, L.-L. Huang, A.-Q. Du, C. Jiang, H. Li and J.-F. Ge, Quercetin alleviates LPS-induced depression-like behavior in rats via regulating BDNF-related imbalance of Copine 6 and TREM1/2 in the hippocampus and PFC, *Front. Pharmacol.*, 2020, **10**, 1544.

18 S. Vas, C. Adori, K. Konczol, Z. Katai, D. Pap, R. S. Papp, G. Bagdy, M. Palkovits and Z. E. Toth, Nesfatin-1/NUCB2 as a potential new element of sleep regulation in rats, *PLoS One*, 2013, **8**, e59809.

19 D. K. Chen, Y. T. So and R. S. Fisher, Use of serum prolactin in diagnosing epileptic seizures, *Neurology*, 2005, **65**, 668–675.

20 G. Wang, Q. Wang, J. Bai, G. Li, K. Tao, G. Wang and Z. Xia, RYGB increases postprandial gastric nesfatin-1 and rapid relieves NAFLD via gastric nerve detachment, *PLoS One*, 2020, **15**, e0243640.

21 I. Lusic, I. Pintaric, I. Hozo, L. Boic and V. Capkun, Serum prolactin levels after seizure and syncopal attacks, *Seizure*, 1999, **8**, 218–222.

22 E. J. Vélez and S. Unniappan, Nesfatin-1 and nesfatin-1-like peptide suppress growth hormone synthesis via the AC/PKA/CREB pathway in mammalian somatotrophs, *Sci. Rep.*, 2020, **10**, 16686.

23 S. Aydin, E. Dag, Y. Ozkan, F. Erman, A. F. Dagli, N. Kilic, I. Sahin, F. Karatas, T. Yoldas, A. O. Barim and Y. Kendir, Nesfatin-1 and ghrelin levels in serum and saliva of epileptic patients: hormonal changes can have a major effect on seizure disorders, *Mol. Cell. Biochem.*, 2009, **328**, 49–56.
24 S. Aydin, E. Dag, Y. Ozkan, F. Erman, A. F. Dagli, N. Kilic, I. Sahin, F. Karatas, T. Yoldas, A. O. Barim and Y. Kendir, Nesfatin-1 and ghrelin levels in serum and saliva of epileptic patients: hormonal changes can have a major effect on seizure disorders, *Mol. Cell. Biochem.*, 2009, **328**, 49–56.
25 S. Himori, S. Nishitani and T. Sakata, Aptamer-based nanofilter interface for small-biomarker detection with potentiometric biosensor, *Electrochim. Acta*, 2021, **368**, 137631.
26 I. Novodchuk, M. Bajcsy and M. Yavuz, Graphene-based field effect transistor biosensors for breast cancer detection: a review on biosensing strategies, *Carbon*, 2021, **172**, 431–453.
27 H. José, N. P. D. Mello, B. Bachour and M. Mulato, Polyaniline-based field effect transistor for DNA/RNA biomarker sensing: comparison to electrochemical impedance and inorganic layer, *Sens. Actuators, A*, 2021, **318**, 112481.
28 N. Masurkar, N. K. Thangavel, S. Yurgelevic, S. Varma, G. W. Auner and L. M. R. Arava, Reliable and highly sensitive biosensor from suspended MoS_2 atomic layer on nano-gap electrodes, *Biosens. Bioelectron.*, 2021, **172**, 112724.
29 S. Xu, T. Wang, G. Liu, Z. Cao, L. A. Frank, S. Jiang, C. Zhang, Z. Li, V. V. Krasitskaya, Q. Li, Y. Sha, X. Zhang, H. Liu and J. Wang, Analysis of interactions between proteins and small-molecule drugs by a biosensor based on a graphene field-effect transistor, *Sens. Actuators, B*, 2021, **326**, 128991.
30 S.-M. Chang, S. Palanisamy, T.-H. Wu, C.-Y. Chen, K.-H. Cheng, C.-Y. Lee, S.-S. F. Yuan and Y.-M. Wang, Utilization of silicon nanowire field-effect transistors for the detection of a cardiac biomarker, cardiac troponin I and their applications involving animal models, *Sci. Rep.*, 2020, **10**, 22027.
31 E. Danielson, M. Dindo, A. J. Porkovich, P. Kumar, Z. Wang, P. Jain, T. Mete, Z. Ziadi, R. Kikkeri, P. Laurino and M. Sowwan, Non-enzymatic and highly sensitive lactose detection utilizing graphene field-effect transistors, *Biosens. Bioelectron.*, 2020, **165**, 112419.
32 E. Danielson, V. A. Sontakke, A. J. Porkovich, Z. Wang, P. Kumar, Z. Ziadi, Y. Yokobayashi and M. Sowwan, Graphene based field-effect transistor biosensors functionalized using gas-phase synthesized gold nanoparticles, *Sens. Actuators, B*, 2020, **320**, 128432.
33 M. Sedki, Y. Chen and A. Mulchandani, Non-carbon 2D materials-based field-effect transistor biosensors: recent advances, challenges, and future perspectives, *Sensors*, 2020, **20**, 4811.
34 A. M. Foudeh, R. Pfattner, S. Lu, N. S. Kubzdela, T. Z. Gao, T. Lei and Z. Bao, Effects of water and different solutes on carbon-nanotube low-voltage field-effect transistors, *Small*, 2020, **16**, 2002875.
35 N. I. Khan, M. Mousazadehkasin, S. Ghosh, J. G. Tsavalas and E. Song, An integrated microfluidic platform for selective and real-time detection of thrombin biomarkers using a graphene FET, *Analyst*, 2020, **145**, 4494.
36 Y. Liang, M. Xiao, D. Wu, Y. Lin, L. Liu, J. He, G. Zhang, L.-M. Peng and Z. Zhang, Wafer-scale uniform carbon nanotube transistors for ultrasensitive and label-free detection of disease biomarkers, *ACS Nano*, 2020, **14**, 8866–8874.
37 H. Wang, Y. Wang, X. Hou and B. Xiong, Bioelectronic nose based on single-stranded DNA and single-walled carbon nanotube to identify a major plant volatile organic compound (p-ethylphenol) released by phytophthora cactorum infected strawberries, *Nanomaterials*, 2020, **10**, 479.
38 W. Kim, J. S. Lee and J. Jang, Aptamer-functionalized three-dimensional carbon nanowebs for ultrasensitive and free-standing PDGF biosensor, *ACS Appl. Mater. Interfaces*, 2020, **12**, 20882–20890.
39 Y. Liu, H. Teng, H. Hou and T. You, Nonenzymatic glucose sensor based on renewable electrospun Ni nanoparticle-loaded carbon nanofiber paste electrode, *Biosens. Bioelectron.*, 2009, **24**, 3329–3334.
40 X. Mao, F. Simeon, G. C. Rutledge and T. A. Hatton, Electrospun carbon nanofiber webs with controlled density of states for sensor applications, *Adv. Mater.*, 2013, **25**, 1309–1314.
41 J. S. Lee, W. Kim, J. Jang and A. Manthiram, Sulfur-embedded activated multichannel carbon nanofiber composites for long-life, high-rate lithium sulfur batteries, *Adv. Energy Mater.*, 2017, **7**, 1601943.
42 K. H. Cho, D. H. Shin, J. Oh, J. H. An, J. S. Lee and J. Jang, Multidimensional conductive nanofilm-based flexible aptasensor for ultrasensitive and selective HBsAg detection, *ACS Appl. Mater. Interfaces*, 2018, **10**, 28412–28419.
43 J. S. Lee, W. Kim, S. Cho, J. Jun, K. H. Cho and J. Jang, Multidimensional hybrid conductive nanoplatebased aptasensor for platelet-derived growth factor detection, *J. Mater. Chem. B*, 2016, **4**, 4447–4454.